



Ocean Feature Monitoring with Wide Swath Synthetic Aperture Radar

Sunny Wu, Antony Liu, Gregory Leonard, and William G. Pichel

By providing better spatial coverage, wide swath synthetic aperture radar (SAR) can offer a more complete picture of various mesoscale ocean features. With better temporal coverage, SAR also supplies crucial information for the tracking and monitoring of these features using, for instance, the technique of two-dimensional wavelet analysis. Examples presented in this article of fronts in the Gulf of Mexico and off the mid-Atlantic coast, an oil spill off Point Barrow, Alaska, and internal waves in the South China Sea illustrate some of the myriad ocean applications that are better observed and monitored with wide swath SAR. (Keywords: Internal wave, Oil spill, Remote sensing, Wavelet transform, Wide swath SAR.)

INTRODUCTION

Wide swath synthetic aperture radar (SAR) modes, such as Radarsat's ScanSAR narrow (50-m resolution, 300-km swath width) and ScanSAR wide (100-m resolution, 500-km swath width), have two major advantages over SAR standard beam modes (25-m resolution, 100-km swath width). First, as the name implies, they offer a wider viewing scope. As such, these modes provide a more complete picture of what is being played out in the viewing area, which often leads to a better identification and more accurate description of the feature or event being imaged. Moreover, a wider viewing scope makes it feasible to compare the SAR data with other spaceborne remote sensing data, such as those collected by scatterometers, infrared imagers, and ocean color imagers, which typically have a much coarser spatial resolution. Comparison of SAR data with the data collected with other imaging mechanisms

can often help to identify the underlying process of the feature or event imaged. Second, wide swath SAR has a shorter repeating cycle, which results in better temporal resolution. Repeat coverage may allow us to track, over the course of several days, a mesoscale feature or event that has a relatively short life span and could not otherwise be monitored. With a 500-km swath width, the Radarsat ScanSAR wide beam can cover most coastal areas in 3 days, making it a powerful tool for coastal monitoring.

By pairing wide swath SAR data with an effective image analyzing tool, such as the technique of two-dimensional wavelet transform used in some of the case studies presented in this article, it is possible to extract useful information from the data in an objective and semi-automated fashion. The wavelet transform essentially works as a highly efficient bandpass filter

that can be used to separate processes with many different scales (temporal or spatial) and provide information on their relative phase or location.¹ Wavelet transforms may be applied to SAR data for many purposes, such as near-real-time screening of data (feature extraction) and data reduction (gray scale image to binary image). This technique has been successfully applied to satellite remote sensing images for coastal monitoring² as well as for ice edge and ice floe tracking in the marginal ice zones and polar oceans.³

In this article, we will first give a brief account of the two-dimensional wavelet analysis that forms the basis of our feature extraction and tracking algorithms. This account is followed by several case studies on fronts, oil spills, and internal waves, which are based primarily on wide swath SAR data, to demonstrate the many applications of these data.

TWO-DIMENSIONAL WAVELET ANALYSIS

The wavelet transform, $W_s(a, \mathbf{b})$, of a function, $s(\mathbf{r})$, where $\mathbf{r} = (x, y)$, is expressed in terms of the complex-valued wavelet function, $w(\mathbf{r})$, as follows (the asterisk represents the complex conjugate):

$$W_s(a, \mathbf{b}) = \frac{1}{a} \int s(\mathbf{r}) w^* \left(\frac{\mathbf{r} - \mathbf{b}}{a} \right) d\mathbf{r} \quad (1)$$

where the wavelet function is dilated by a factor a and shifted by \mathbf{b} . Variables in bold in Eq. 1 are vectors, while those in italics are scalars. The function $w(\mathbf{r})$ is the basic wavelet that must satisfy the admissibility condition but is otherwise subject to choice within certain limits. Thus, the continuous wavelet transform ensures energy conservation. For data analysis, the mother wavelets often used are a Gaussian-modulated sine and cosine wave packet (the Morlet wavelet) and the Laplacian of a Gaussian function (the latter is also known as the Mexican Hat wavelet). In this study, the analyzing wavelet is chosen as the Laplacian of a two-dimensional Gaussian function, a real-valued function. The basic wavelet has the following form:

$$w(x, y) = \left[2 - (x^2 + y^2) \right] \exp \left(-\frac{x^2 + y^2}{2} \right). \quad (2)$$

Since convolution is commutative with respect to differentiation, the resulting wavelet transform yields the Laplacian of a Gaussian-smoothed original function. As a result, the wavelet-transformed image is a differential

image with accentuated amplitude change. Its zeroes thus correspond to the inflection points of the original function. The contours of zero crossing indicate the edges in the pattern of the input function. In addition, the Mexican Hat wavelet has a closed form so that it can be used directly for computation without the use of a recursive scheme to generate the wavelet base functions. In practice, the wavelet transform is carried out by making use of the fast Fourier transform algorithm and the following relationship to ensure computational efficiency:

$$WT(s) = \text{IFFT}[\text{FFT}(s) \cdot \text{FFT}(w)], \quad (3)$$

where s is the original signal, w is the wavelet function, WT denotes the wavelet transform, FFT is the fast Fourier transform, and IFFT is the inverse fast Fourier transform. Equation 3 holds because of the convolution property.

Specifically, to apply the wavelet transform for image analysis, one must first find a suitable a , which corresponds to the length scale of the Laplacian-of-a-Gaussian wavelet. A proper a value is chosen based on two factors: (1) the length scale of the feature of interest, and (2) the resolution (or pixel spacing) of the original image. A threshold value is then selected for differential detection to be carried out. In this step, the pixel locations of significant differentials are determined so that the feature of interest can be delineated from the background.

SOME CASE STUDIES

Front in the Gulf of Mexico

A ScanSAR narrow image taken on 23 November 1997 over the Gulf of Mexico reveals a distinct, nearly straight front stretching at least 300 km in length. The center of the front in this scene is some 400 km southwest of New Orleans. Figure 1 shows the front delineated by the two-dimensional wavelet analysis. The 50-m pixel subscene was first block-averaged using a 4×4 pixel kernel and was then subjected to the wavelet transform. The wavelets used in this analysis are the Laplacian and the first derivatives of a two-dimensional Gaussian. The spatial scale used in the wavelet transform is 16, corresponding to 3.2 km in physical dimension. The resulting frontal delineation should resolve any spatial structure greater than 3.2 km while ignoring the smaller spatial variations.

To get a sense of how strong the contrast in backscatter really is across the front, the gray value is profiled (Fig. 2) along a transect normal to the frontal boundary (see Fig. 1). Between pixel numbers 225 and

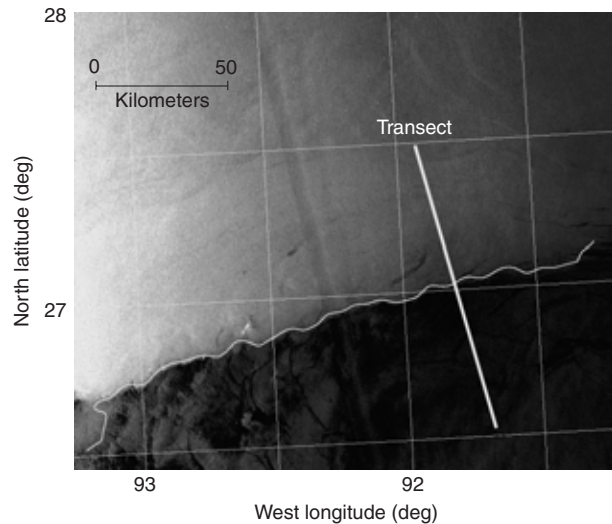


Figure 1. A subsene from a Radarsat ScanSAR narrow beam image collected over the Gulf of Mexico on 23 November 1997 (© Canadian Space Agency [CSA], 1997). The front has been delineated by the wavelet analysis. Notice the surface-film-like features in the lower left corner.

275, the gray value drops noticeably, signaling the existence of a front. The value changes from an average of 35 on the brighter side to an average of 15 on the darker side.

Closer inspection reveals some curious features in this scene. For instance, there are many surface-film-like filaments on the south side of the front, which seem to suggest that the front has a biological origin. It is known that a phytoplankton bloom can take place over an expansive area (on the order of 100×100 km) and can be captured by spaceborne remote sensing instruments, as was the case in the Coccolithophorid bloom in the east Bering Sea in September–October 1997 and again on 25 April 1998 as observed by the SeaWiFS (Sea-viewing Wide Field-of-View Sensor) (personal communication, Charles McClain, NASA Goddard Space Flight Center, Oceans and Ice Branch, Greenbelt, MD, 1998). It is believed that the phytoplankton bloom generally takes on the appearance of petroleum oil slicks. If so, since the ScanSAR narrow mode has a wide swath (300 km), it should be able to capture such an event if the sensor is turned on at the right moment and the right place. Is the front in question really of biological origin? Or is it caused by a difference in other physical properties such as sea surface temperature or surface wind?

Examination of nearly concurrent SeaWiFS and Advanced Very High Resolution Radiometer (AVHRR) imagery (not shown) effectively rules out biological causes. Comparison between SAR data and EDAS (Eta Data Assimilation System) wind data from the (U.S.) National Center for Environmental Prediction (Fig. 3) provides a much more plausible explanation. On 23

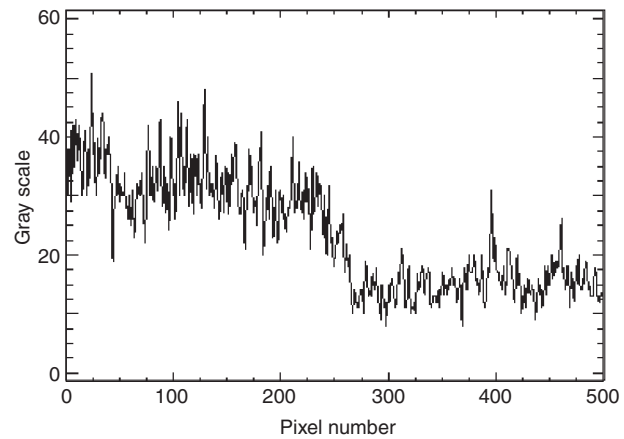


Figure 2. Gray value profile along the transect indicated in Fig. 1.

November at about the same time the SAR image was collected, the wind pattern as seen in the wind vector plot of Fig. 3 displays an abrupt change in the vicinity of the front, from ≈ 8 m/s out of north-northeast on the north side to ≈ 4 m/s out of east-southeast on the south side. Two mechanisms may be responsible for the existence of the front: (1) the change in wind speed, which causes a contrast in sea state, and (2) the accumulation of natural surface films brought about by the convergence around the front, which was in turn caused by the $\approx 90^\circ$ shift in wind direction.

One can estimate the change in σ_0 resulting from the change in wind speed using the following formula:⁴

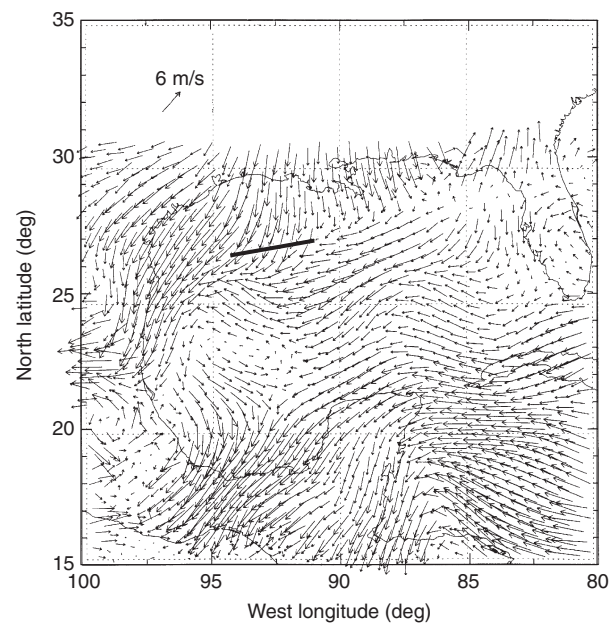


Figure 3. Eta Data Assimilation System (EDAS) wind vector diagram with 48-km resolution over the Gulf of Mexico. The heavy black line indicates the approximate position of the front observed in the SAR image.

$$\sigma_0(U) = CU^\gamma, \quad (4)$$

where $\sigma_0(U)$ is the backscatter value in dB, U is the surface wind speed, and C and γ are empirical coefficients determined to be -29.7 and 1.5 , respectively. The resulting $\Delta\sigma_0$ caused by the wind speed change is thus estimated as 65%, or more than twice as large as that derived from the SAR data. The discrepancy may be explained by two facts. First, the ScanSAR data used in this study are uncalibrated; as with most ScanSAR data from Radarsat to this date, data values are relative rather than absolute. Since the calculation of σ_0 depends on the absolute values of the data, the uncalibrated data therefore may have a bias for this kind of quantitative estimate. Second, Eq. 4 holds under the assumption that wind is the sole controlling factor of the sea surface roughness. This assumption, though, breaks down in many circumstances, for instance, in the presence of surface films, which may occur frequently in coastal waters, as happened in this case.

Front off the Mid-Atlantic Coast

A nearly circular feature, having distinct boundaries on the north and the south and a less distinguishable boundary on the west, was observed off the mid-Atlantic coast in two consecutive Radarsat ScanSAR narrow beam scenes collected on 11 May 1997. The feature was centered at 38.5°N , 66.5°W with a north-south extent of approximately 355 km. A mosaic of the two scenes is shown in Fig. 4. The location of this feature is too far away from the Gulf Stream for it to be generated by shear as a spin-off eddy. Its sheer size also makes it an unlikely candidate for an eddy of some sort. On the other hand, it is known that an intense low-pressure system can make a striking signature on the wide swath SAR image with a pronounced and well-defined “eye” in the center, as do polar lows in the Bering Sea and hurricanes in the Atlantic.⁵ (See Vachon et al., this issue; Friedman and Li, this issue.) This near-circular feature, though, does not have a center that remotely resembles an eye. If neither an oceanic eddy nor an intense atmospheric low-pressure system, then what is the underlying process that is responsible for this frontal feature?

In an attempt to uncover the nature of this frontal feature, the NSCAT (NASA scatterometer aboard the Japanese Advanced Earth Observing Satellite) ocean wind data with 25-km resolution was acquired and subsequently overlaid on top of the SAR mosaic (Fig. 4). It becomes abundantly clear that the northern boundary is a result of wind forcing change. There is a pronounced difference in both wind speed and direction across the boundary. The wind field just north of the northern boundary has an average speed of 5.6 m/s and average direction of 261° , while just within

the boundary it has an average speed of 10.3 m/s and average direction of 281° . According to Eq. 4, the wind speed change would result in a 60% change in backscattering intensity (σ_0), large enough to make the front visually distinguishable. The relative change estimated in σ_0 based on the SAR data, however, is far off in this case, amounting to only 6%. It should be pointed out that the gray values used here to calculate σ_0 are again relative values. For a fixed gray scale difference of 15, as in this case, for instance, one can make the relative change in σ_0 vary widely from 1 to 100% by simply adding a different constant to the gray scale. This reminds us to use special caution when interpreting numerical results that are based on uncalibrated data.

Unlike the northern boundary, which can be explained by the wind difference, the change in wind speed along the southern boundary is not evident. However, the wind pattern (Fig. 4) does suggest a convergent zone on one side (lower left corner) and a divergent zone on the other side (lower right corner) of the front. We speculate that the accumulation of natural surface films brought about by the convergence

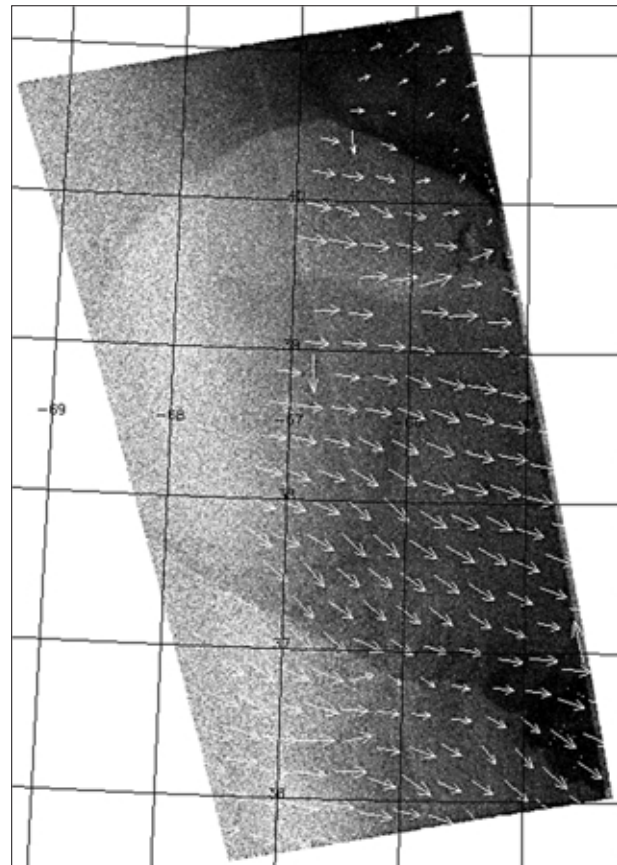


Figure 4. A mosaic of two consecutive Radarsat ScanSAR narrow beam images (© CSA, 1997), overlaid with the same-day surface NASA scatterometer (NSCAT) wind data.

of surface drift may be responsible for the darker appearance in the convergent zone.

Oil Spills off Point Barrow, Alaska

The reason oil spills are distinguishable on radar images is that surface films have a dampening effect on short surface waves and thereby make the sea surface smoother. Radar is remarkably sensitive to changes in the surface roughness. The smoother sea surfaces in oil-covered areas take on a darker appearance in radar imagery, much like that of low wind areas. Often it is

their distinctive shapes and sharper boundaries that distinguish oil from low wind.

In early November 1997, the ScanSAR wide beam captured an oil spill off Point Barrow, Alaska. Oil slicks show up clearly on the Radarsat ScanSAR imagery on 2, 3, and 9 November. The oil spill may have originated from a vessel that appears in the image on 2 November. Three subscenes of 1024×1024 pixels with 100-m resolution containing the oil slicks were cropped from each of the original images for further analysis.

Among the three ScanSAR subscenes (Figs. 5a–5c), the oil slicks on 2 November have the most isotropic

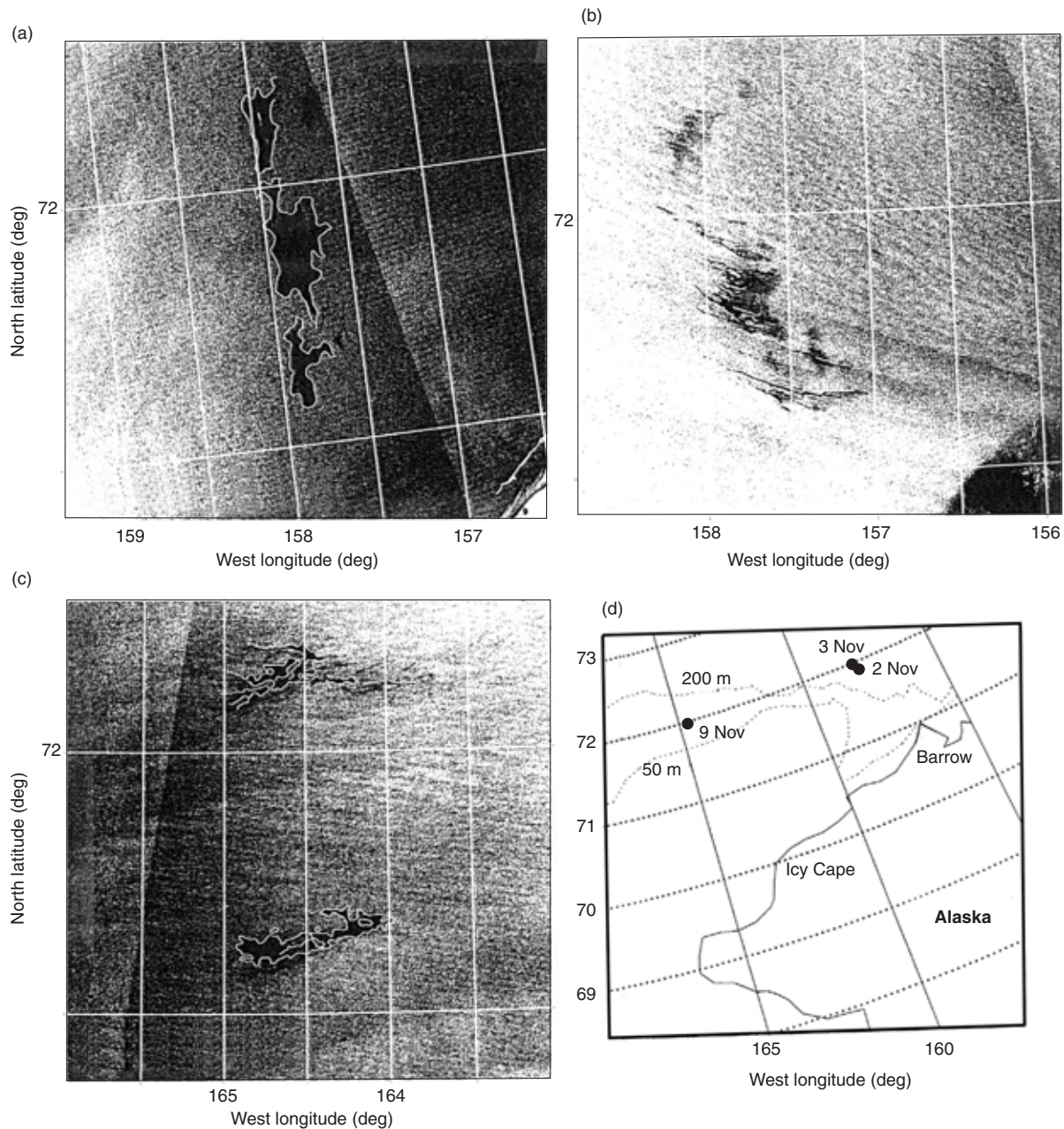


Figure 5. Subscenes from Radarsat ScanSAR wide beam images showing patches of oil slicks delineated by the wavelet analysis on (a) 2 November, (b) 3 November, and (c) 9 November 1997. (d) Map showing approximate locations of the oil slicks on the 3 days.

shape, indicating that diffusion is in control, evidently as the result of low wind and calm sea. The matching a value for the wavelet analysis is 8, corresponding to a length scale of 800 m. Figure 5a shows the result of wavelet analysis with the oil slicks delineated. The oil spill appears as three separate patches that line up in the north–south direction.

On 3 November the wind had obviously become stronger, with wind streaks clearly visible (Fig. 5b). The wind streaks from the SAR image suggest that the wind is blowing out of the southeast. As a result, the oil slick had broken into a series of elongated patches in the direction of the wind. The oil slick patches are no longer well-defined as was the case just 1 day earlier. A much smaller a ($a = 2$) is used in this case in order to separate the oil slicks from the background. This value corresponds to a length scale of 200 m.

Six days later, on 9 November, the oil slick had drifted farther offshore to the west, becoming two barely recognizable fuzzy patches. Figure 5c shows a subscene from the SAR image collected on 9 November, with the oil slick delineated with the wavelet analysis. The a value used in this case is 4, corresponding to a spatial scale of 400 m. Figure 5d shows a map of Point Barrow and its vicinity, with the approximate locations of the oil slicks represented by black dots for all 3 days.

Internal Waves in the South China Sea

SAR data from Radarsat and the European Remote Sensing satellites ERS-1 and ERS-2 have been regularly collected and used to study the characteristics of internal waves in the East and South China Seas.^{5,6} From the SAR imagery, rank-ordered packets of internal waves are often seen propagating westward in the South China Sea, in the area from Luzon Strait all the way west onto the continental shelf. The internal waves observed in this region are enormous both in their crest length (over 200 km) and amplitude (as much as 100 m). Those waves are typically generated by the branch-out of the Kuroshio current across the Luzon Strait. Assuming the internal waves have a semidiurnal tidal origin,^{7,8} the group speed can be estimated.

There are basically two opposite types of nonlinear internal waves: (1) elevation waves where the displacement of the thermocline is upward and (2) depression waves where the displacement is downward. According to internal wave theory, the ratio between the surface mixed-layer depth and the bottom-layer depth determines which type of internal waves may evolve. If the ratio is greater than 1, i.e., the surface mixed layer is thicker than the bottom layer, then internal waves of the elevation type may exist. Otherwise, only waves of the depression type may be present. In SAR imagery, as a result of vertical flow patterns induced by the associated internal waves, a depression wave packet is

characterized by a bright band (a rough surface caused by subsurface convergence), followed immediately by a dark band (a smooth surface caused by subsurface divergence) on its leading edge. The pattern reverses for the elevation wave packet. On the basis of the observations from SAR imagery, most of the internal waves in the South China Sea are of the depression type, particularly in summer.⁶ This finding is consistent with theory since the surface mixed layer is generally thinner than the bottom layer over the entire region in summer. During the rest of year, though, the mixed layer may become thicker than the bottom layer in shallower water if surface wind, and the subsequent wind-induced mixing, is sufficiently strong, a condition that could harbor internal waves of the elevation type.

Wide swath SAR, such as ScanSAR, has the capability of capturing a series of internal wave packets that might have been triggered by successive tidal cycles. This makes it an excellent tool for observing the evolution of internal waves. Figure 6 shows just one such example. In this scene, four internal wave packets are seen propagating westward. Dongsha Island (which appears as a bright dot) and the coral reefs to its east (which appear as a dark half circle) happen to be on their path. The distance between adjacent wave packets decreases progressively from about 100 km (between

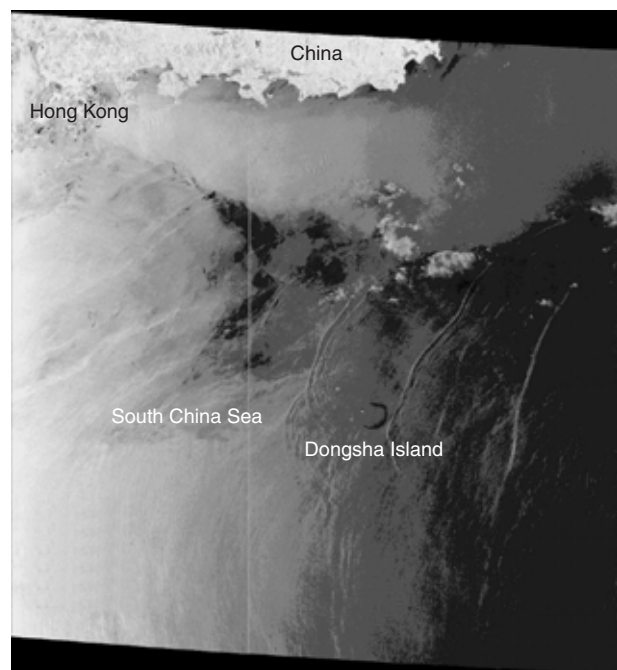


Figure 6. Radarsat ScanSAR image collected over the northern part of the South China Sea on 26 April 1998 showing at least four packets of internal waves: one approaching the Dongsha coral reefs, one diffracted by the reefs and becoming two separate sets of wave packets upon exiting (the curvatures of these two packets suggest that their paths will cross at a later time), and a fourth propagating westward. North is toward the top of the figure; image dimensions are 528 × 478 km. (© CSA.)

the first and second wave packets from the right) to 50 km (between the third and fourth wave packets) as the internal waves move onto the continental shelf, indicating a shoaling effect. In addition, one can see that the internal wave packet diffracted and split into two sets of separate wave packets upon passing Dongsha Island.

The ScanSAR wide beam image in Fig. 7 provides another interesting example in which the effect of a depth change on the evolution of nonlinear internal waves can be plainly observed. In this scene (collected on 4 May 1998), one can see two packets of depression waves in deep water on the right, the second being right around the location of the shelf break where the water depth is about 500 m, and one elevation wave packet in the shallower water on the left where the depth is about 220 m. Assuming that the surface-layer depth changes little from deep water to shallower water, the theory would require the thickness of the surface mixed layer to be in the range of 110 to about 200 m. The conductivity/temperature/depth measurements at this location 15 days later on 19 May 1998 indeed indicate that the mixed-layer depth is in the range of 100–120 m (personal communication, Joseph Wang, National Taiwan University, Department of Oceanography, Taipei, 1998), which agrees with the estimate based on observation from ScanSAR data.

CONCLUDING REMARKS

Remote sensing with rapid repeat coverage is by far the most efficient way to monitor and study the



Figure 7. A subsense from a Radarsat ScanSAR image collected in the same area as in Fig. 6 on 4 May 1998. There are three westward-propagating internal wave packets in this subsense. An eastward-propagating internal wave packet east of Dongsha Island is also faintly visible. The depression waves (the first wave packet from the right) have changed their polarization upon passing a critical point and have become elevation waves (the first wave packet from the left) in shallower water. North is toward the top of the figure. Horizontal dimension = 528 km. (© CSA.)

marine environment. The mapping of mesoscale oceanic feature in the coastal zone is a potentially important application for spaceborne SAR data. Wide swath SAR data, such as the ScanSAR data from Radarsat, are particularly suitable for this purpose. The use of SAR data to track oceanic features such as eddies, fronts, ice edges, and river and estuarine plumes can certainly aid in the management of fisheries and coastal waters, especially in areas like Alaskan coastal waters, where the sea surface tends to be uniformly cold and clouds occur regularly, making AVHRR measurements and ocean color observations much less usable.

One reason to use wavelet analysis to analyze remote sensing data is that the amount of the data is often overwhelmingly large. The wavelet transform of satellite images can be used for several purposes, such as near-real-time screening (feature extraction) and data reduction (gray scale image to binary image). In this study, we have demonstrated that wavelet analysis using the Laplacian-of-a-Gaussian as the basic wavelet is a useful tool in extracting and tracking oceanic features.

Apart from SAR's unique capability of operating under all weather and lighting conditions, the wide swath SAR is particularly useful in that it provides not only a better spatial coverage, which makes the comparison between SAR and other types of remote sensing data feasible, but also a better temporal resolution, which is crucial for feature or event tracking. Both points have been substantiated in the collection of case studies presented in this article. Wind fronts observed in ScanSAR can be validated with NSCAT and meteorological data. Because of the wide swath, the depression and elevation internal waves have been observed in the same Radarsat SAR image. Furthermore, the internal wave speed estimated from sequential packets in the SAR image can be used to determine the thickness of the mixed layer. The tracking of oil spills has been demonstrated by using sequential ScanSAR images. The wide swath SAR has proven to be a useful and promising tool for both coastal management and basic research. One can imagine that with a more rapid repeating cycle the wide swath SAR will inspire more applications in both communities.

REFERENCES

- Combes, J. M., Grossman, A., and Tchamitchian, Ph. (eds.), *Wavelet: Time Frequency Methods and Phase Space: Proc. Int. Conf., Marseille, France*, Springer-Verlag, New York (1989).
- Liu, A. K., Peng, C. Y., and Chang, S. Y-S., "Wavelet Analysis of Satellite Images for Coastal Watch," *IEEE J. Oceanic Eng.* **22**, 9–17 (1997).
- Liu, A. K., Martin, S., and Kwok, R., "Tracking of Ice Edge and Ice Floes by Wavelet Analysis of SAR Images," *J. Atmos. Oceanic Technol.* **14**, 1187–1198 (1997).
- Keller, W. C., Wisman, V., and Alpers, W., "Tower-Based Measurements of the Ocean C-band Radar Backscattering Cross Section," *J. Geophys. Res.* **94**(C1), 924–930 (1989).

- ⁵Liang, N. K., Liu, A. K., and Peng, C. Y., "A Preliminary Study of SAR Imagery on Taiwan Coastal Water," *Acta Oceanogr. Taiwanica* **34**, 17–28 (1995).
- ⁶Liu, A. K., Chang, Y. S., Hsu, M. K., and Liang, N. K., "Evolution of Nonlinear Internal Waves in China Seas," *J. Geophys. Res.* **103**, 7995–8008 (1998).
- ⁷Liu, A. K., Apel, J. R., and Holbrook, J. R., "Nonlinear Internal Wave Evolution in the Sulu Sea," *J. Phys. Oceanogr.* **15**, 1613–1624 (1985).
- ⁸Liu, A. K., "Analysis of Nonlinear Internal Waves in the New York Bight," *J. Geophys. Res.* **93**, 12,317–12,329 (1988).

ACKNOWLEDGMENTS: We thank the Canadian Space Agency (CSA) for providing Radarsat SAR images; copyright of these data is owned by CSA. The study on the internal waves in the South China Sea is in collaboration with Professor Ming-Kuang Hsu of the National Taiwan Ocean University. We also thank Drs. Chuanmin Hu and Frank Muller-Karger of the University of South Florida for providing us with the AVHRR and SeaWiFS images for the Gulf of Mexico, and Dr. Eugene Wei of NOAA for providing us with the EDAS wind data

for the Gulf of Mexico. This research was supported by the National Aeronautics and Space Administration, the National Oceanic and Atmospheric Administration Coastal Ocean Program, and the Office of Naval Research.

THE AUTHORS

SUNNY WU, ANTONY LIU, and GREGORY LEONARD are at NASA Goddard Space Flight Center, Greenbelt, MD. Their e-mail addresses are sunny@neptune.gsfc.nasa.gov, liu@neptune.gsfc.nasa.gov, and greg@kaon.gsfc.nasa.gov, respectively.

WILLIAM G. PICHEL is with the NOAA/NESDIS Office of Research and Applications, Camps Springs, MD. His e-mail address is wpichel@nesdis.noaa.gov.